

Analysis of surface deformation prediction in high mountain canyon areas based on time-series InSAR technology and improved Elman neural network

Kuayue Chen¹, Wenfei Xi², Baoyun Wang^{1,3}

5 ¹School of Mathematics, Yunnan Normal University, Kunming, People's Republic of China

²Faculty of Geography, Yunnan Normal University, Kunming, People's Republic of China

³Yunnan Key Laboratory of Modern Analytical Mathematics and Applications, Kunming, People's Republic of China

Correspondence to: Baoyun Wang (wspbmly@163.com)

Abstract. Mountain canyon areas often have complex terrain and unstable geological conditions, making them prone to
10 disasters such as landslides and debris flows. Surface deformation is an early sign of these disasters, and accurate
prediction of deformation can help detect potential hazards in advance, reducing the likelihood of disaster occurrence.

To address the issues of over-reliance on deformation data and model singularity in existing surface deformation prediction
methods in high mountain canyon areas, this study proposes the improvement of Elman neural network using cuckoo search
algorithm and grey wolf optimization algorithm (CS-Elman and GWO-Elman) from the perspective of multi-temporal and
15 multi-factor analysis. Firstly, surface deformation in the study area is monitored using SBAS-InSAR and PS-InSAR
techniques. Then, the optimal evaluation factors are determined from 13 evaluation factors including digital elevation model
(DEM) and slope using grey correlation analysis and correlation matrix analysis in SPSSAU software. These optimal factors,
combined with surface deformation monitoring values obtained from InSAR technology, are used to construct CS-Elman
and GWO-Elman prediction models from a multi-factor and multi-temporal perspective. Finally, the optimal prediction
20 model is determined through comparative experiments and its prediction performance is validated. Results indicate: (1)
SBAS-InSAR and PS-InSAR techniques have a strong correlation ($R^2 = 0.85$) in monitored deformation rates, confirming
their potential for joint analysis. (2) The CS-Elman model outperforms the GWO-Elman model, achieving a lower error
range, faster convergence (3 iterations), and better metrics (MSE: 0.020 mm/a, MAE: 1.620 mm/a, MAPE: 21.500%). (3)
Compared to SVM, LSTM, and PSO-BP models, the CS-Elman model has the smallest error range (0.071–1.843 mm/a) and
25 better accuracy (MAE 0.818 mm/a, MAPE 9.353%). (4) The CS-Elman model excels in short-term predictions but is less
effective for long-term forecasting. It predicts a maximum surface uplift of 120.913 mm, offering insights for disaster
prevention.

Keywords. Small baseline subset interferometric synthetic aperture radar (SBAS-InSAR); Persistent scatterer
interferometric synthetic aperture radar (PS-InSAR); Elman neural network; Deformation monitoring; Predictive analysis;
30 Geological hazard

1 Introduction

China is prone to geological disasters, which have caused significant losses to lives and property security of its people (Derbyshire 2001; Xu and Wang 2022; Liu and Wang 2024). Landslides, debris flows, and collapses, common in mountainous and canyon areas, are highly hazardous due to their suddenness and hidden nature (Jiang et al. 2022; Guo et al. 2016). Therefore, Monitoring and early warning in these regions are essential for identifying risks and taking measures to reduce disaster likelihood and minimize losses (An et al. 2022).

Surface deformation directly reflects the stability and movement of slopes, providing crucial information for identifying geological risks such as landslides and debris flows (Wang et al. 2020; Tao et al. 2021). Traditional methods like the global positioning system (GPS) (Kim et al. 2003) and leveling measurements (Vanicek et al. 1980) have limitations in accuracy, workload, and terrain adaptability, and are ineffective for large-scale monitoring (Yang et al. 2020; He et al. 2022). In contrast, interferometric synthetic aperture radar (InSAR) technology possesses all-weather and all-day characteristics. It enables the direct spatial acquisition of extensive and high-precision terrain elevation and deformation information (Osmanoğlu et al. 2016; Zhang et al. 2022; Zhang et al. 2022). Currently, Many researchers have used InSAR for monitoring natural disasters (Nikolaeva et al. 2014; Huang, Liu, and Liu 2019; Suresh and Yarrakula 2020; Yang et al. 2023). On the contrary, in terms of surface deformation prediction, the majority of studies are based on constructing prediction models using time-series deformation data, with only a few adopting a model-building approach from the perspective of deformation influencing factors. Ye et al. (2022) analyzed the spatiotemporal characteristics of ground deformation along the Zhengzhou subway line using PS-InSAR technology. They then utilized inverse distance interpolation and equalization processing and applied a long short-term memory (LSTM) model to predict and analyze typical deformation points. Their findings validated that compared to grey models, the LSTM model exhibits higher fitting and prediction accuracy. Among them, the grey model is a forecasting method used for small samples and uncertain systems, mainly applied to solve prediction problems with incomplete information and sparse data. Yang et al. (2022) utilized InSAR technology to monitor the deformation information of the Meili Snow Mountain Glacier from 2020 to 2021. They established a prediction model based on genetic algorithm-back propagation (GA-BP) neural networks and found that the optimized prediction model significantly improved accuracy. Teng et al. (2022) utilized SBAS-InSAR surface deformation monitoring data from the Hefei City to construct training samples. They established an Elman model and experimental results showed that the predicted deformation values of the Elman model were in basic agreement with the monitoring values. Radman et al. (2021) combined InSAR with environmental factors to predict land deformation using ensemble models. Wang et al. (2019) utilized SBAS-InSAR technology to acquire surface deformation characteristics in the Erhai Lake region from 2015 to 2018. They selected building area, water level, rainfall and temperature as inputs to the back propagation (BP) neural network for predicting surface deformation. Although the aforementioned methods can effectively combine InSAR technology and neural network

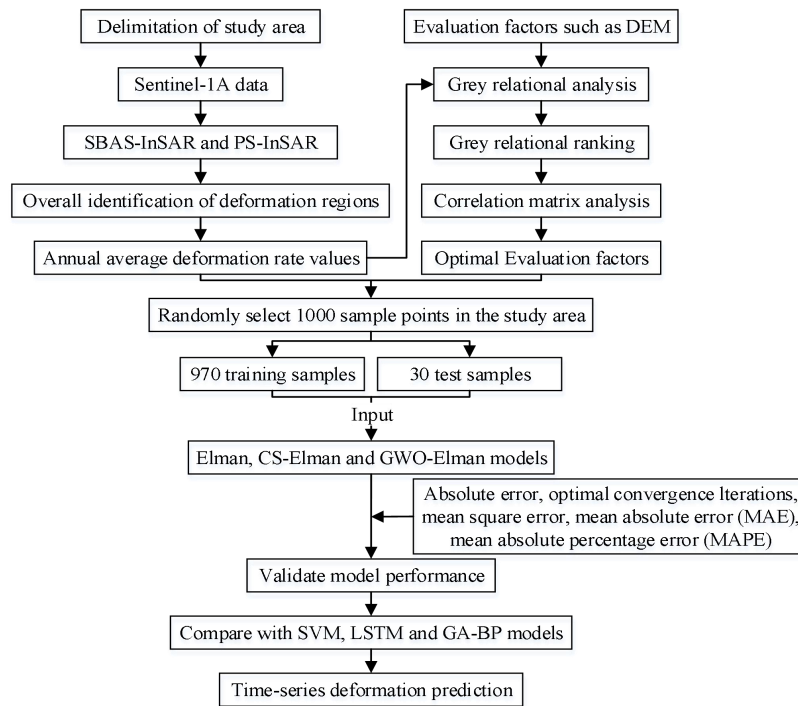
models to monitor and predict surface deformation information, they all have certain drawbacks and limitations. Some scholars (Teng, Wang, and Jiang 2022; Yang et al. 2022; Ye et al. 2022) propose prediction models that overly rely on deformation data, considering fewer other factors that may trigger disasters. They only utilize deformation data as the input and output layers for prediction, which presents certain shortcomings. If a model is based solely on deformation data, its lack of multi-factor analysis capability will limit its prediction accuracy and comprehensiveness. Deformation data typically reflect slow changes, making it difficult to predict sudden disasters such as debris flows and landslides. Additionally, other scholars (Wang et al. 2019; Radman, Akhoondzadeh, and Hosseiny 2021) construct prediction models from the perspective of influencing factors, but the prediction accuracy of these models is relatively low, primarily due to insufficient optimization of the weights and thresholds of the network model. To enhance model performance, it is necessary to introduce optimization algorithms, such as Cuckoo Search (CS) and Grey Wolf Optimization (GWO), to better optimize network parameters.

In high mountain canyon areas, surface deformation exhibits nonlinear characteristics, leading to the complexity of natural disasters such as landslides and debris flows. Merely utilizing time-series deformation data as input for prediction models often yields unsatisfactory results in studying surface deformation in disaster-prone areas. Therefore, it is essential to consider major causative factors influencing deformation, such as slope, soil type and vegetation coverage. Additionally, surface deformation prediction typically involves a set of data correlated with time series. Hence, selecting appropriate prediction models can effectively enhance prediction accuracy. The Elman neural network is a typical type of local regression network. It adds a feedback layer acting as a delay operator to the basis of the BP neural network, enabling it to memorize information and thereby adapt to time-varying characteristics. This improvement enhances the network's global stability, providing significant advantages when handling time-series foundational data such as surface deformation (Ding et al. 2013; Jia et al. 2019). However, determining the weights, thresholds and learning rates of the Elman neural network is often challenging, requiring optimization. The cuckoo search (CS) algorithm (Mareli and Twala 2018) and grey wolf optimizer (GWO) algorithm (Gupta and Deep 2019) are chosen to search for the optimal weights, thresholds and learning rates of the Elman neural network, aiming to enhance the model's prediction accuracy for surface deformation variables.

In summary, this study utilizes time-series InSAR technology and an improved Elman neural network algorithm to monitor and predict surface deformation in high mountain canyon areas. It proposes a predictive model constructed from multiple time-series and factors. Specifically, the study processes the research area using InSAR technology to obtain subsidence areas and annual deformation rate maps. These are combined with relevant influencing factors as input layers, while the annual deformation rate serves as the output layer, establishing the relationship between influencing factors and deformation rate prediction models.

2 Research Methodology

This study first uses SBAS-InSAR and PS-InSAR techniques to obtain surface deformation information in the study area. Then, the optimal evaluation factors are selected based on correlation analysis. Next, the optimal evaluation factors are used as inputs for the CS-Elman and GWO-Elman models, with the annual average deformation rate as the output. The output results are compared with the annual average deformation rate obtained from InSAR technology to verify the model's accuracy. Finally, the optimal model is applied for future time series deformation prediction. The overall technical process is shown in Figure 1.



100 **Figure 1: Overall technical flowchart.**

2.1 Acquisition of surface deformation information in the study area

Due to the lack of precise measurement data such as leveling measurements and GPS, many scholars have already verified the reliability of Sentinel-1A data quality (Ye et al. 2022; Li, Dai, and Zheng 2024). The study utilizes the SBAS-InSAR and PS-InSAR techniques available in the Sarscape 5.6.2 module of ENVI 5.6.2 software to process Sentinel-1A images and extract deformation information in the study area. This study firstly employs SBAS-InSAR technology (Berardino et al. 2002) to extract surface deformation information in the study area, and then utilizes PS-InSAR technology (Ferretti et al. 2001) to extract deformation variables for validation. By comparing and correlating the deformation results obtained from the two techniques, detailed information regarding surface deformation in the study area is obtained.

110 The SBAS-InSAR technology provides large-scale continuous spatial deformation results, while the PS-InSAR technology provides deformation information for individual pixel points. Utilizing surface deformation information obtained from

different time-series InSAR technologies can complement each other, resulting in more accurate and comprehensive monitoring results.

2.2 Selection of evaluation factors

115 Surface deformation is influenced by multiple factors, which exhibit diversity and complexity. Moreover, certain factors may exhibit correlations, and high correlations can lead to model complexity and reduced operational speed. Therefore, conducting correlation analysis among various factors is crucial. By analyzing the correlations among factors, it is possible to exclude highly correlated factors, which is significant for model establishment and surface deformation monitoring (Ulusay, Türeli, and Ider 1994).

120 Based on the geological environmental background of the study area, this study selects factors closely related to the formation of debris flows, including digital elevation model (DEM) data, slope, aspect, curvature, soil type, topographic wetness index (TWI) (Sørensen, Zinko, and Seibert 2006), stream power index (SPI) (Parker and Davey 2023), surface roughness, terrain relief, fractional vegetation cover (FVC), rainfall, lithology and vegetation type, as factors for surface deformation in the study area. In which, TWI is an index that reflects the influence of terrain on water accumulation and

125 distribution, primarily used to describe the potential moisture conditions of an area. SPI is based on the combination of slope and flow, and is mainly used to analyze the erosion and scouring strength of water flow on the surface. First, the ArcGIS software is used to extract the raster data of each factor in the study area. Next, the SPSSAU software is employed to conduct grey relational analysis on the 13 factors with the deformation values monitored by InSAR technology separately, obtaining the grey relational degree ranking, and selecting factors with high correlation to the deformation values. Grey

130 relational analysis is a method within grey system theory that aims to reveal the relationships between different factors or variables by analyzing their similarity. The basic concept is that if two sequences have more similar trends in variation, their degree of correlation is higher. Finally, the bivariate correlation analysis tool is used to analyze the correlation matrix of the above factors, eliminating highly correlated factors and obtaining the optimal evaluation factors. Bivariate correlation analysis is a statistical method used to measure the strength and direction of the relationship between two variables. By

135 calculating the correlation coefficient, the linear relationship between the two variables can be quantified. The results can help determine whether there is a positive correlation (both variables increase or decrease together), a negative correlation (one variable increases while the other decreases), or no correlation (no obvious relationship between the two variables). The correlation coefficient R is used to measure the degree of correlation between each factor, selecting more suitable factors to construct CS-Elman and GWO-Elman models with the deformation values. The value range and correlation of R are shown

140 in Table 1.

Table 1: Range of R values and correlation table.

Correlation coefficient	Range of values	Correlation
R	(0,1]	Positive correlation
	0	No linear correlation
	[-1,0)	Negative correlation
$ R $	(0,0.5]	Low correlation
	(0.5,0.8]	Significant correlation
	(0.8,1]	High correlation

2.3 Construction of improved Elman network model

145 2.3.1 Elman neural network

The Elman neural network, a type of recurrent neural network (RNN), incorporates a feedback layer into its structure, consisting of an input layer, a hidden layer, a feedback layer and an output layer (Elman 1990). With the presence of the feedback layer, the Elman network can retain previous information relative to conventional neural networks, making it more suitable for processing sequential data. It can better capture the temporal characteristics and dependencies in the data. **This**
150 **makes it particularly effective in handling tasks with time-series characteristics, such as surface deformation.** The structure of the Elman neural network is illustrated in Figure 2.

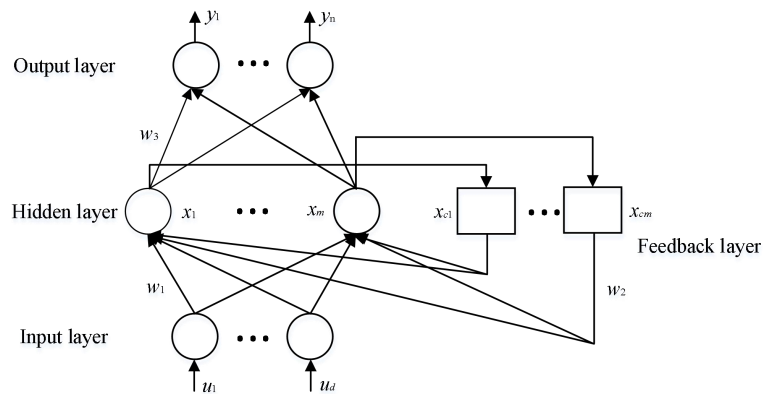


Figure 2: Elman neural network structure.

155

In this representation, $[u_1, u_2, \dots, u_d]$ represents the input vector; $[x_1, x_2, \dots, x_m]$ represents the hidden layer node vector; $[x_{c1}, x_{c2}, \dots, x_{cm}]$ represents the feedback layer node vector; and $[y_1, y_2, \dots, y_n]$ represents the output vector. w_1 , w_2 and w_3 denote the connection weights from the input layer to the hidden layer, from the feedback layer to the hidden layer, and from the hidden layer to the output layer, respectively.

160 The mathematical model of the Elman neural network is as follows in equations (1) to (3):

$$y(k) = g[w_3 x(k) + b_2] \quad (1)$$

$$\mathbf{x}(k) = f[\mathbf{w}_2 \mathbf{x}_c(k) + \mathbf{w}_1 \mathbf{u}(k-1) + \mathbf{b}_1] \quad (2)$$

$$\mathbf{x}_c(k) = \mathbf{x}(k-1) \quad (3)$$

In the equations, k represents any given moment; $\mathbf{y}(k)$ represents the network output; $\mathbf{x}(k)$ represents the hidden layer output; $\mathbf{u}(k)$ represents the external input; \mathbf{b}_1 and \mathbf{b}_2 are the thresholds for each layer; g and f represent the transfer functions of the output neurons and hidden layer neurons, respectively.

2.3.2 Cuckoo search algorithm

The cuckoo search (CS) algorithm, proposed by Yang et al. (2009) in 2009, is a population-based optimization algorithm. It features simplicity in design, requiring fewer parameters, and is insensitive to parameter changes, exhibiting good stability. It is less likely to get stuck in local optima and is applicable to both continuous and discrete optimization. The characteristics of nest-parasite behavior observed in cuckoos inspire the algorithm's approach: cuckoos lay their eggs in other birds' nests, relying on host birds to incubate them; if a host discovers the foreign egg, it will abandon the nest. The algorithm's steps can be summarized as follows: (1) Each cuckoo lays one egg at a time during breeding and randomly selects a nest to lay the egg. (2) In each nest, only the highest-quality eggs are retained to breed the next generation. (3) The number of parasitic nests is fixed, and if a host bird discovers a foreign egg, the nest is abandoned.

The *Levy* flight of cuckoos is a biological description used in the updating process of the cuckoo search algorithm to avoid falling into local optima. The flight formula of cuckoos is represented in equation (4):

$$\mathbf{x}_i^{t+1} = \mathbf{x}_i^t + \alpha \oplus Levy(\lambda) \quad (4)$$

In the equation, \mathbf{x}_i^t represents the position of the i th nest at generation t , where $i=1,2,\dots,n$. α denotes the step size, which is a positive number typically set to 1. \oplus denotes pointwise multiplication. $Levy(\lambda)$ is the random search path, generating step sizes that follow a Levy distribution, as shown in equation (5):

$$Levy(\lambda) \sim u = t^{-\lambda}, 1 < \lambda \leq 3 \quad (5)$$

The characteristic of *Levy* flight is that the step size is random. Larger step sizes can ensure a certain probability of escaping from local optima, thus obtaining the global optimum solution.

2.3.3 Grey wolf optimizer algorithm

The grey wolf optimizer (GWO) algorithm is a population-based metaheuristic algorithm proposed by Mirjalili et al. (2014) in 2014, inspired by the social hierarchy of grey wolf populations. In the social hierarchy of grey wolves, there are four different types of wolves, including α , β , δ and ω wolves, with their social status decreasing from left to right. The four ranks of wolf packs represent the four solutions searched during the GWO optimization process, representing the optimal solution, good solution, suboptimal solution and candidate solution, respectively.

The GWO algorithm mainly consists of three steps: encircling, hunting and attacking. The behavior of grey wolves can be defined in mathematical models, as shown in equations (6) and (7):

$$D = \left| C \cdot X_p(t) - X(t) \right| \quad (6)$$

$$X(t+1) = X_p(t) - A \cdot D \quad (7)$$

195 In the equations, D represents the distance between the grey wolf and the prey; A and C are coefficient vectors, which can be calculated respectively by equations (8) and (9); t denotes the iteration number; $X_p(t)$ and $X(t)$ represent the position vectors of the prey and the grey wolf after t iterations, respectively; $X(t+1)$ denotes the position vector of the grey wolf after $t+1$ iterations.

$$A = 2a \cdot r_1 - a \quad (8)$$

200
$$C = 2 \cdot r_2 \quad (9)$$

In the equations, r_1 and r_2 are random vectors within the range $[0,1]$; a is the convergence factor, which linearly decreases from 2 to 0 as the number of iterations increases, calculated as shown in equation (10):

$$a = 2 - \frac{2t}{T_{\max}} \quad (10)$$

In the equation, T_{\max} represents the maximum number of iterations.

205 2.3.4 CS/GWO-Elman neural network

Elman neural network demonstrates outstanding performance in handling time-series data and tasks related to time. But it also suffers from issues such as vanishing gradients, slow training speeds and susceptibility to local minima. **Specifically: (1) The initial values of neural network weights have a significant impact on the training process. If the initial weights are not properly chosen, the network may get stuck in a local optimum or experience slow convergence. The search for the best weight combination in high-dimensional space is complex, and efficient optimization algorithms are needed to find the global optimum. (2) Thresholds in neural networks play a crucial role in adjusting the output. Like weights, the choice of thresholds affects network performance and convergence speed. Thresholds also need to be optimized to ensure that the network performs well on training data and can effectively generalize to new data. (3) Learning rate determines the step size for updating network weights. If the learning rate is too large, the training process may oscillate or fail to converge. 215 Conversely, if the learning rate is too small, the training process will be slow. Dynamic adjustments to the learning rate may be required during different stages of training, making the choice of an appropriate learning rate and adjustment strategy critical. Optimization algorithms, such as genetic algorithms (GA), particle swarm optimization (PSO), grey wolf optimization (GWO), and cuckoo search (CS), can more effectively search for the optimal combination of weights, thresholds, and learning rates, thus improving the overall performance of the network. The optimization process can also**

220 help prevent overfitting and enhance the model's generalization ability, ensuring better performance on unseen data. To address these challenges, this paper utilizes CS and GWO algorithms to optimize the initial weights and thresholds of Elman network. The CS algorithm uses a random search method to find the optimal solution. In neural network training, CS helps optimize the network's weights and thresholds, thereby improving the model's prediction accuracy. GWO gradually approaches the optimal solution by introducing the search mechanisms of elite wolves and random wolves. The GWO
 225 algorithm is used to adjust the parameters of the Elman neural network, enabling it to find a better-performing solution in a shorter time. These optimized parameters are then applied to the Elman neural network, ultimately producing values that meet the required accuracy. The workflow is illustrated in Figure 3.

The specific steps of the CS-Elman neural network are as follows:

Step 1: Divide the data into training and testing sets, and the data is normalized using the mapminmax function. Specifically,
 230 the inputs of the training set $[u_1, u_2, \dots, u_d]$ are normalized to the range $[0, 1]$ according to equation (11), while the outputs of the training set $[y_1, y_2, \dots, y_n]$ are normalized to the range $[-1, 1]$ according to equation (12).

$$u'_i = \frac{u_i - u_{\min}}{u_{\max} - u_{\min}}, \quad (11)$$

$$y'_j = 2 \times \frac{y_j - y_{\min}}{y_{\max} - y_{\min}} - 1, \quad (12)$$

In the equations, $u'_i (i=1,2,\dots,d)$ represents the normalized data, while u_i is the original data, with u_{\min} and u_{\max} being the minimum and maximum values in $[u_1, u_2, \dots, u_d]$, respectively. Similarly, $y'_j (j=1,2,\dots,n)$ represents the normalized data, while y_j is the original data, with y_{\min} and y_{\max} being the minimum and maximum values in $[y_1, y_2, \dots, y_n]$, respectively.

235 Step 2: Construct the Elman neural network, select relevant data as input and output, and initialize the weights and thresholds of the neural network.

Step 3: Given the number of nests n , randomly generate n nests $X_0 = (x_1^0, x_2^0, \dots, x_n^0)^T$ within a given range, where the relevant variables represent the weights and thresholds of the neural network. During the training process, optimize these parameters to find the optimal nest positions x_b^0 .

240 Step 4: Utilize the Levy flight method to update the nest positions, generating new nests $X_0 = (x_1^t, x_2^t, \dots, x_n^t)^T$. Calculate the fitness of the new nests and compare them with the previous generation. If the fitness of the new nests is better, update their positions; otherwise, retain the positions of the previous generation.

Step 5: Generate a new solution F_i and compare it with the candidate solution F_j . If $F_j > F_i$, do not update the nest positions; if $F_i > F_j$, update the nest positions. When updating the nest positions, also compare them with the positions of the previous
 245 generation. Retain the new nest positions if they are better; otherwise, do not change the nest positions.

Step 6: Return the parameters of nest positions that meet the iteration limit or error condition to the Elman neural network as the optimal weights and thresholds. Finally, the predicted results are reverse normalized using Equation (13) to obtain the

original data range of the test set outputs.

$$\bar{y}_j = y_j' \times (y_{\max} - y_{\min}) + y_{\min}, \quad (13)$$

In the equation, y represents the final predicted results.

250 The specific steps of the GWO-Elman neural network are as follows:

Steps 1 and 2 are the same as those in the CS-Elman neural network.

Step 3: Set the parameters of the GWO algorithm, including the number of grey wolves in the population, the upper and lower bounds of the grey wolf dimensions, the dimensions of individual grey wolf position information and the maximum number of iterations.

255 Step 4: Select the fitness function, calculate the fitness, and select the optimal wolf (α), the superior wolf (β) and the inferior wolf (δ).

Step 5: Update the positions of the remaining wolves (ω), and update the parameters A , C and a .

Step 6: Map the position of the optimal wolf (α) that meets the iteration count or error condition to the weight matrix and return it to the Elman neural network as the optimal weights and thresholds.

260

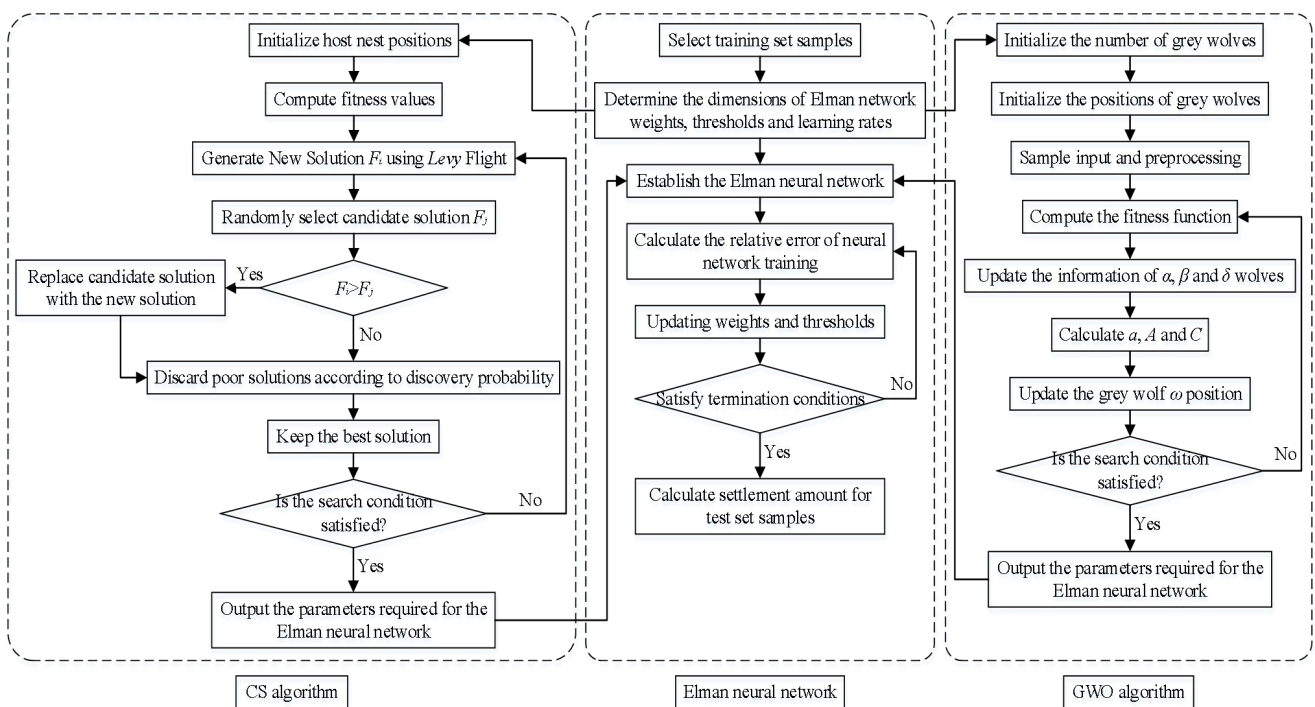


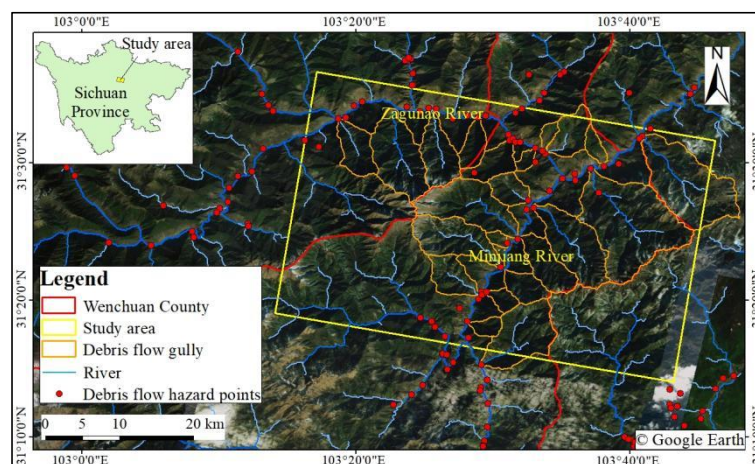
Figure 3: CS-Elman and GWO-Elman neural network flowchart.

3 Study area and data sources

265 3.1 Study area

The high mountain canyon area of the Minjiang River Basin is located in Wenchuan County, Sichuan Province, China. It is a typical high-risk area for geological disasters, particularly frequent debris flows and landslides. This basin was affected by the M_s 8.0 earthquake on May 12, 2008 (Dong et al. 2008), leading to a substantial increase in debris sources in the valley and an unusually intense activity of debris flows. Prior to the earthquake, there were no records of debris flow disasters in the valley, but in recent years, there have been several large-scale debris flows. The occurrence of debris flows in this area is closely related to rainfall and belongs to rainfall-induced landslide debris flows. This type of debris flow is initiated by heavy rainfall-induced slope movement, leading to the formation of debris flows (Zhou et al. 2014).

This study selects the mountainous canyon areas along both sides of the Minjiang River and Zagunao River as the study area. The river valley depression forms a "V"-shaped canyon with the Minjiang River as the boundary, representing a typical high mountain canyon. The location of the study area is shown in Figure 4. The terrain in this area is steep, with a maximum elevation difference of 4185 meters. This extreme elevation variation makes the mountains prone to gravity-induced landslides and debris flows. Due to the low vegetation cover and concentrated rainfall during the rainy season, severe soil erosion occurs in the area. The soil in certain localities is loose, especially after being disturbed by seismic activity, making the soil layers even more unstable and highly susceptible to landslides and the formation of debris flows during heavy rainfall. Its unique terrain and geological structure result in frequent heavy rainfall, loose soil, and severe soil erosion. Consequently, geological disasters occur frequently in this area. Debris flow disasters have occurred in multiple valleys due to short-term heavy rainfall on July 10, 2013, August 20, 2019 and June 26, 2023, respectively (Ding and Huang 2019; He et al. 2022; Zhang et al. 2023). Through field investigations of geological disasters, historical data, and visual interpretation of remote sensing images, a total of 25 debris flow occurrences were identified within the study area. Their specific distribution is shown in Figure 4.



290 **3.2 Data sources**

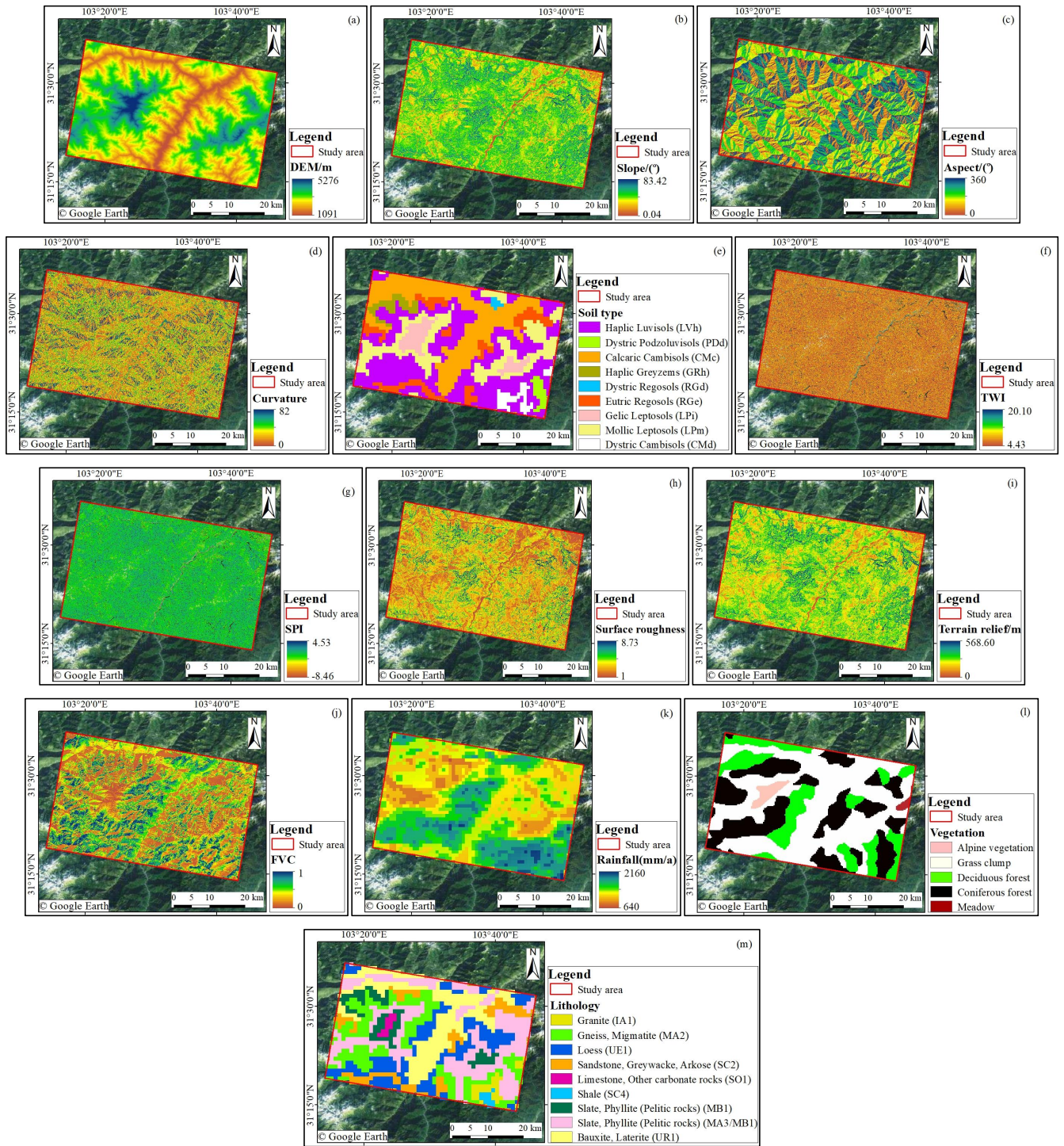
The data mainly used in this study are 30 scenes of Sentinel-1A descending data from January 24, 2022 to December 21, 2023 downloaded from the Alaska satellite facility (ASF) (Shankar et al. 2023). The data are acquired in interferometric wide (IW) mode, providing single look complex (SLC) images with a swath width of 250 km. The polarization mode is vertical-vertical (VV), with an incidence angle (angle between the transmission direction and the vertical direction) of 40.98°.

295 The revisit period is 12 days, and the spatial resolution is 5 m*20 m (range*azimuth), which is used to obtain the time-series deformation information of the study area.

The auxiliary data include precise orbit determination (POD) data used to correct orbit information and improve the accuracy of image orbits, digital elevation model (DEM) data used to eliminate the influence of terrain phase in interferometric phase (Liao et al. 2013), google satellite images as auxiliary reference images, DEM, slope, aspect, curvature, soil type, TWI, SPI, 300 surface roughness, terrain relief, FVC, rainfall, lithology and vegetation type used as evaluation factors for constructing predictive models. The data sources are shown in Table 2. In the text, "1.07 m" represents the pixel resolution of Google Earth. The basic information of various data types is illustrated in Figure 5. The unit "mm/a" for rainfall represents millimeters per year.

305 **Table 2: Data source parameter table.**

Name of data	Temporality of data	Spatial resolution	Source of data
Sentinel-1A	Descending orbit from January 24, 2022 to December 21, 2023	5 m*20 m	Alaska satellite facility (ASF)
POD	Sentinel-1A image generation 21 days later	None	European space agency
DEM	In 2018	30 m	Japan aerospace exploration agency (JAXA)
Google satellite images	January 14, 2024	1.07 m	Bigemap map downloader
Lithology and vegetation	In 2008	90 m	International soil reference and information centre
Slope, aspect, curvature, TWI, SPI, surface roughness and terrain relief	In 2018	30 m	Processed using ArcGIS to obtain DEM
Soil type	In 2009	90 m	National cryosphere desert data center
FVC	In 2019	30 m	Using ArcGIS to process Landsat 8-9 OLT/TIRS C2 L2 data downloaded from the Geospatial Data Cloud
Rainfall	January 2022 to December 2023	30 m	National earth system science data



310

Figure 5: Layers of various factors. (a) DEM. (b) Slope. (c) Aspect. (d) Curvature. (e) Soil type. (f) TWI. (g) SPI. (h) Surface roughness. (i) Terrain relief. (j) FVC. (k) Rainfall. (l) Vegetation. (m) Lithology. Source of optical background image: © Google

315

Earth (Image capture date: January 14, 2024).

4 Experimental results and analysis

4.1 Surface deformation monitoring experiment

Selecting the primary image in InSAR technology is crucial, and the following three factors should be considered: (1) Temporal stability: The primary image should be chosen at a suitable time point within the monitoring period, typically selecting an image from the middle of the period. This ensures that subsequent images have shorter temporal baselines relative to the primary image, reducing atmospheric effects and temporal decorrelation issues. (2) Surface features: The surface features in the image should be stable. Avoid selecting an image from dates when large-scale surface changes occurred, such as after major natural disasters (e.g., earthquakes, floods, landslides), as they can negatively affect the interferogram. (3) Data quality: The quality of the image is a key factor in selecting the primary image. Ensure that the chosen image has no significant noise, data loss, or other disturbances. Taking into account the aforementioned factors, the two time-series InSAR techniques select April 1, 2023 and December 26, 2022 as the master images, respectively. The annual average deformation rates in the radar line of sight (LOS) direction for the study area from January 24, 2022 to December 21, 2023 are shown in Figures 6 and 7, respectively. Positive values indicate uplift of the Earth's surface, meaning deformation towards the satellite's direction, while negative values indicate subsidence, meaning deformation away from the satellite's direction.

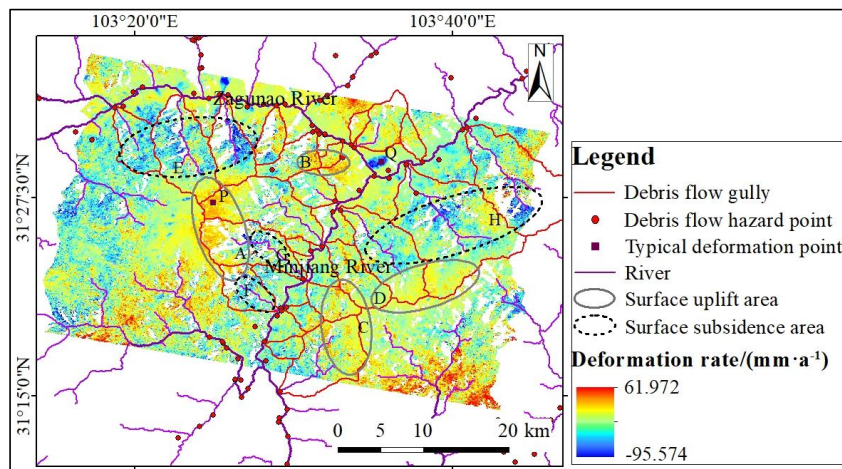
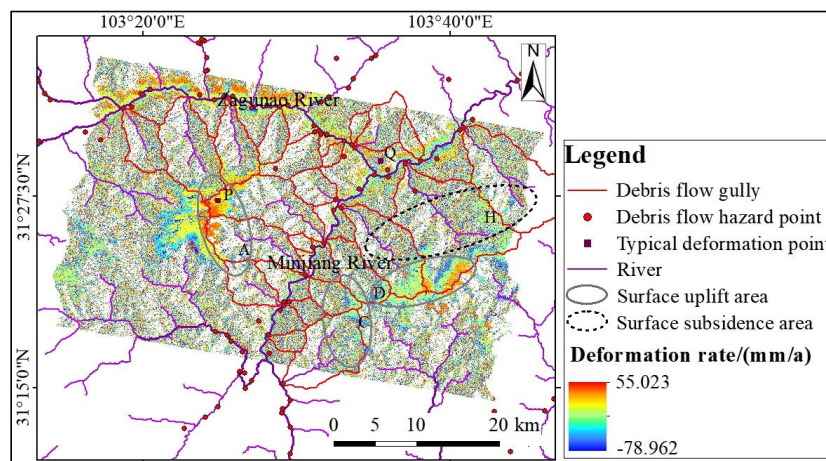


Figure 6: Annual average deformation rate map based on SBAS-InSAR.



335

Figure 7: Annual average deformation rate map based on PS-InSAR.

In Figure 6, the SBAS-InSAR monitoring shows uplift in the upstream areas of various debris flow gullies, such as regions A, B, C and D, with the maximum uplift rate reaching 61.972 mm/a, located at the top of the main gully of Banzi Gully, indicated by point P in the figure. Additionally, different degrees of uplift are observed in the Zagunao River and Minjiang River channels. In the downstream areas of each debris flow gully, subsidence phenomena are observed, as seen in regions E, F, G and H, with the maximum subsidence rate reaching -95.574 mm/a, located at the confluence of the Minjiang and Zagunao rivers, indicated by point Q in the figure. In Figure 7, the PS-InSAR technology monitors the overall deformation rate in the study area, ranging from -78.962 mm/a to 55.023 mm/a. The monitoring effect is less satisfactory compared to

345 SBAS-InSAR technology in areas with low coherence, resulting in fewer retrieved deformation information and greater influence from the geographical environment of the study area. However, PS-InSAR detects deformation patterns similar to those observed with SBAS-InSAR, such as uplift in regions A and D, as well as in the Zagunao River and Minjiang River channels, and subsidence in region H. According to field investigations, a debris flow disaster occurred on June 26, 2023 due to short-duration heavy rainfall, resulting in significant sediment deposition and uplift observed in the river channels.

350 For the typical deformation points P and Q, combined with rainfall data, a comparison of deformation trends is shown in Figure 8. Both time-series InSAR techniques monitor deformation points with roughly consistent trends exhibit nonlinear deformation patterns that correlate with rainfall and display seasonal variations. At point P, uplift increases with increasing rainfall, showing a distinct acceleration process. At point Q, the deformation trend is relatively flat during the rainy season, and as the rainy season recedes, the subsidence rate begins to accelerate. Moreover, the influence of rainfall on ground

355 deformation is temporary, and after rainfall stops, the surface deformation will gradually return to the normal consolidation process.

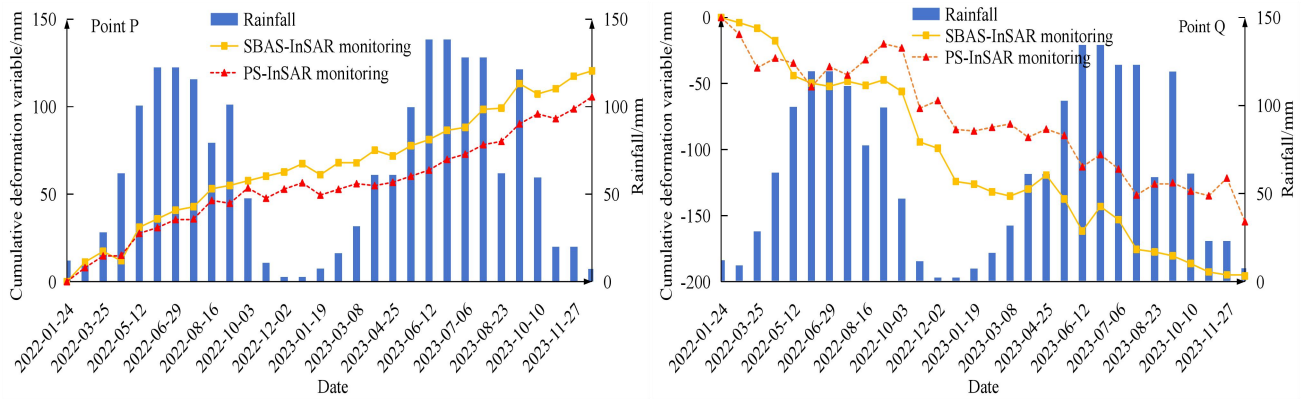


Figure 8: Comparison of deformation trends of typical deformation points monitored by two types of time-series InSAR techniques.

360

Although there are numerical and spatial differences in the final deformation rate results obtained from the two time-series InSAR techniques, their deformation trends are generally consistent. To validate the reliability of the data, a cross-validation method was employed to verify the data before analysis. 300 points with the same name were randomly selected in the study area, and the annual average deformation values monitored by SBAS-InSAR and PS-InSAR techniques were taken as the x and y axes, respectively, for linear regression analysis. The results are shown in Figure 9. The correlation coefficient $R^2=0.85$ between the LOS deformation rates of the same-named points monitored by the two data sets indicates a high correlation between the data monitored by the two InSAR techniques, demonstrating the feasibility of joint analysis using both techniques (Liu et al. 2023).

370

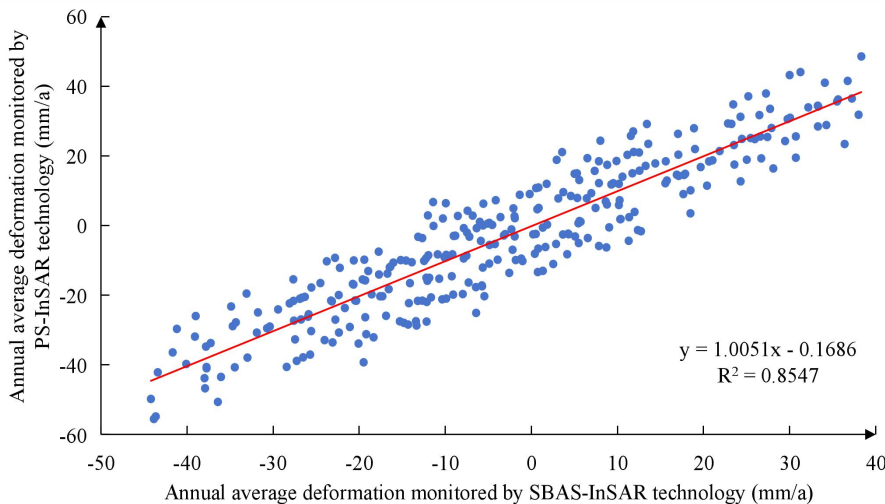


Figure 9: Cross validation results of LOS deformation rate using time series InSAR technology.

In addition, the study area has high vegetation coverage, causing scattering, occlusion and interference of radar signals along the propagation path, leading to severe decorrelation and affecting the accuracy of deformation monitoring. Therefore, the

375

FVC is introduced to analyze the vegetation coverage in the study area. For areas with an FVC greater than 0.6, the deformation points are not selected to eliminate the influence of high vegetation coverage on deformation monitoring in the study area.

4.2 Surface deformation prediction experiment

380 4.2.1 The impact of CS/GWO algorithm on the performance of Elman network

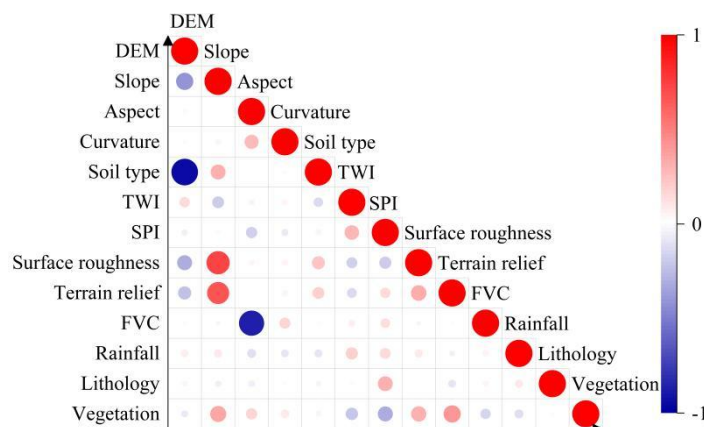
In this study, ArcGIS software is used to extract the layer data of 13 evaluation factors in the research area. In order to assess whether these 13 evaluation factors are suitable as predictors for surface deformation in high mountain gorges, grey relational analysis is conducted using SPSSAU software to analyze the grey relational values between each of the 13 factors and the annual average deformation values monitored by the InSAR technology. The grey relational values are presented in

385 Table 3.

Table 3: The grey relational coefficient between each factor and the deformation value.

Evaluation factor	Grey relational values	Evaluation factor	Grey relational values
DEM	0.809	Surface roughness	0.804
Slope	0.803	Terrain relief	0.789
Aspect	0.803	FVC	0.806
Curvature	0.804	Rainfall	0.807
Soil type	0.779	Lithology	0.794
TWI	0.786	Vegetation	0.825
SPI	0.799		

The grey relational values indicate a high degree of correlation between the selected 13 evaluation factors and the deformation values. However, the final factors have not yet been selected. In order to obtain the optimal evaluation factors to prevent problems such as overfitting and instability caused by strong correlations between factors, a correlation matrix analysis is conducted on each factor (Dziuban and Shirkey 1974). The results are shown in Figure 10.



From Figure 10, it can be observed that the correlation coefficients $|R|$ between DEM and soil type, slope and surface roughness, terrain relief, and aspect and FVC are greater than 0.5, indicating strong correlations. Therefore, highly correlated influencing factors are removed. Consequently, DEM, slope, curvature, TWI, SPI, FVC, rainfall, lithology and vegetation type are selected as evaluation factors for the CS/GWO-Elman model.

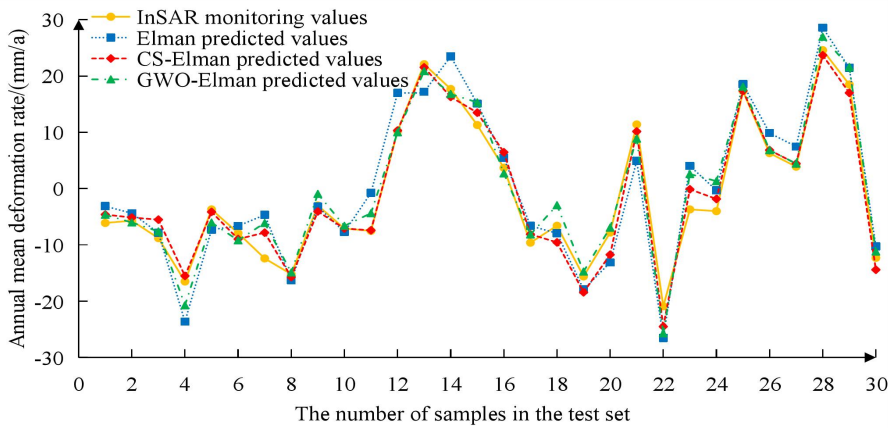
To construct a CS/GWO-Elman model using the nine selected evaluation factors and the average annual deformation rate values extracted by InSAR technology in the study area. Using the Create Random Points tool in ArcGIS, 1000 points are randomly selected as samples for the CS/GWO-Elman neural network, and predictions for 30 sample points are made. To ensure the comparability of the Elman networks optimized by CS and GWO, Matlab software is used to construct the CS/GWO-Elman network models with unified parameters. The chosen training function is trainlm, and tanh and purelin serve as the activation functions for the hidden and output layers, respectively. Trainlm trains feedforward neural networks using the Levenberg-Marquardt algorithm, known for fast convergence, robustness, and excellent performance in handling small to medium-sized problems. Tanh is a hyperbolic tangent function commonly applied in hidden layer nodes to enable the network to learn and approximate nonlinear functions, while purelin is a linear activation function typically employed in the output layer for regression tasks. The network training parameters are detailed in Table 4.

Table 4: CS/GWO-Elman network training parameters.

Parameter names	Setting values	Parameter names	Setting values
Training epochs	1000	Maximum evolutionary generations	50
Learning rate	0.01	Initial population size for CS	10
Minimum training target error	10^{-5}	Probability of discovering a cuckoo egg by CS	0.25
Display frequency	25	Number of searching wolves in GWO	20
Momentum factor	0.01	Range of searching for wolves in GWO	30

The randomly selected samples are input into the Elman, CS-Elman and GWO-Elman models, and their predicted results are compared with the annual average deformation rate results monitored by InSAR, as shown in Figure 11. It can be clearly seen that the predicted curves of the three network models are generally consistent with the InSAR monitoring curve. By calculating the absolute error between the predicted values of each model and the monitored values of InSAR, as shown in Figure 12, the absolute error ranges of Elman, CS-Elman and GWO-Elman models with InSAR monitoring of the annual average deformation rate are 0.205 to 7.733 mm/a, 0.016 to 4.576 mm/a and 0.193 to 6.292 mm/a, respectively. The absolute error range of the CS-improved Elman network is smaller. It is also evident that the absolute error curve of the CS-Elman prediction is closer to the horizontal axis and has a smaller amplitude, indicating better prediction results. Therefore, for

unknown areas of surface deformation, the CS-Elman model predicts surface deformation more effectively by utilizing evaluation factors such as DEM, potentially reducing the time and technical costs associated with InSAR technology.



425

Figure 11: Comparison of the predicted values from the three models with the monitored values from InSAR.

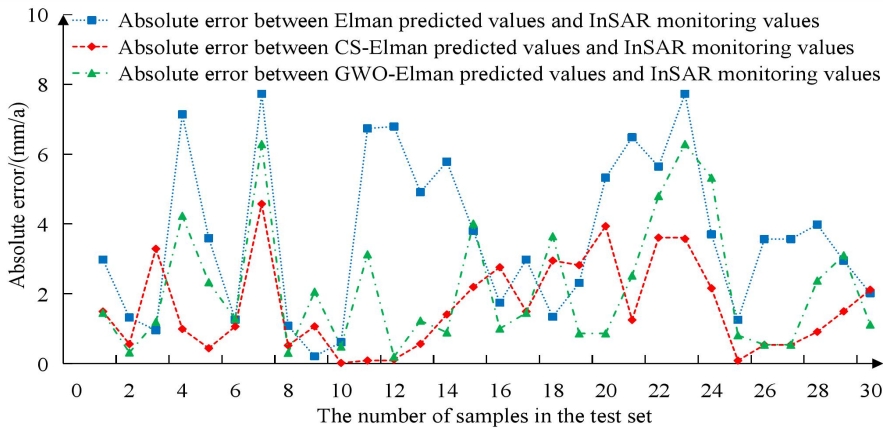


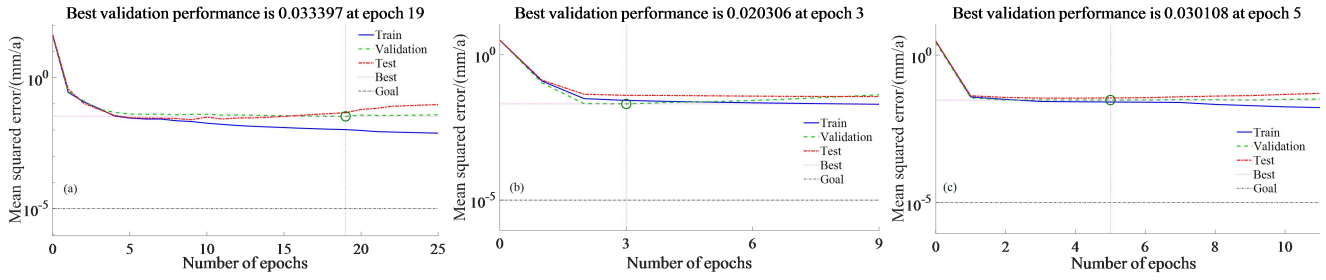
Figure 12: Comparison of absolute errors among three models.

430

To validate the predictive performance under different optimization algorithms, the mean squared error (Hodson, Over, and Foks 2021) and the optimal number of iterations for each group are calculated, as shown in Figure 13. In this figure, validation refers to the model's performance on the validation set during training. The validation set is used to evaluate the model's generalization ability and to avoid overfitting. It shows how the error (such as mean squared error) on the validation data changes as training progresses. Best indicates the model's optimal state during training, which is the moment when the lowest error on the validation set is achieved. It represents the model parameters that perform best on the validation set in the current training. Goal refers to the target error for training, which is typically a threshold set by the user. When the model's error drops to this target value, training can be terminated early, indicating that the desired outcome has been achieved. The optimal convergence iterations for Elman, CS-Elman and GWO-Elman networks are 19, 3 and 5 times, respectively, with mean squared errors of 0.033, 0.020 and 0.030 mm/a, respectively. The Elman network improved by CS converges faster

440

with a smaller mean squared error, validating that the CS algorithm can overcome the slow convergence and low learning rate of Elman neural networks.



445 **Figure 13: Mean square error and optimal iteration numbers of the three models. (a) is Elman model, (b) is CS-Elman model, (c) is GWO-Elman model.**

To validate the reliability of prediction accuracy under different optimization algorithms, the mean absolute error (MAE) (Chai and Draxler 2014) and mean absolute percentage error (MAPE) (De et al. 2016) are used as evaluation metrics. The smaller the values of these evaluation metrics, the smaller the prediction error of the model, indicating a better fit to the data. MAE represents the average of the absolute errors between the InSAR monitoring values and the corresponding model predicted values, calculated using the formula as equation (14). Here, n denotes the number of samples, y_i represents the InSAR monitoring values, and \hat{y}_i represents the predicted values of the corresponding network.

$$MAE = \frac{1}{n} \sum_{i=1}^n |y_i - \hat{y}_i| \quad (14)$$

455 MAPE represents the mean absolute percentage difference between the InSAR monitoring values and the corresponding model predicted values, calculated using the formula as equation (15):

$$MAPE = \frac{1}{n} \sum_{i=1}^n \left| \frac{y_i - \hat{y}_i}{y_i} \right| \times 100\% \quad (15)$$

The comparison of evaluation indicators for each group of data is shown in Table 5. Through comparison, it is found that both CS and GWO algorithms can effectively improve the prediction performance and accuracy of the Elman network. Moreover, the CS-Elman model has smaller MAE and MAPE, indicating higher prediction accuracy. Thus, it is demonstrated that utilizing the CS algorithm to improve the Elman neural network leads to better prediction performance and accuracy for surface deformation in high mountain gorges.

Table 5: Comparison of evaluation metrics for the three models.

Evaluation indicators	Elman	CS-Elman	GWO-Elman
MAE/(mm/a)	3.650	1.620	2.155
MAPE/%	44.663	21.500	29.689

4.2.2 Model comparison analysis experiment

To further verify the superiority of the CS-Elman model in predicting surface deformation in high mountain gorges, we select the SVM, LSTM and GA-BP (Yang et al. 2022) models and compared them with the CS-Elman model in a comparative experiment. In the comparative experiment, we use the same 9 factors including DEM and the time-series of annual average deformation rates extracted by InSAR technology as data. To reduce the randomness of the experimental results and ensure a more comprehensive and reliable evaluation of the model's performance, 507 sample data points are randomly reselected. Among these, 500 are used as training samples, and the remaining 7 are used for prediction. The prediction results of each model after training are shown in Figure 14, the absolute errors between the predicted values and the InSAR monitoring values are shown in Figure 15, and the performance comparison is shown in Table 6.

475

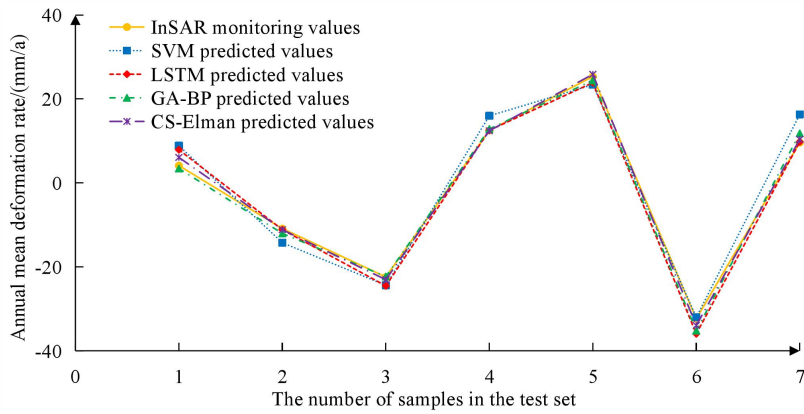
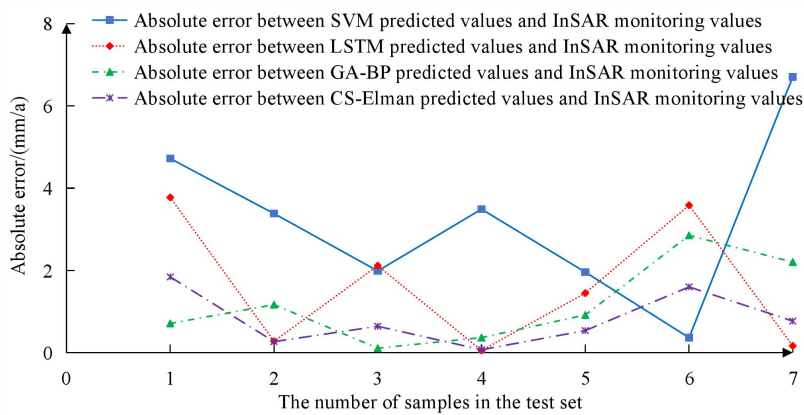


Figure 14: Comparison between the predicted values of each model and the monitored values from InSAR.



480 Figure 15: Absolute error between predicted values of each model and the monitored values from InSAR.

Table 6: Comparison of performance metrics for each model.

Model	Evaluation indicators			
	MAE/(mm/a)	MAPE/%	Convergence optimal iteration times	Mean squared error/(mm/a)
SVM	3.231	37.241%	23	0.031
LSTM	1.631	17.458%	10	0.033
GA-BP	1.189	9.521%	7	0.029
CS-Elman	0.818	9.353%	3	0.024

In Figure 14, the predicted curves of each model align closely with the InSAR monitoring curve. As shown in Figure 15 and
485 Table 6, the prediction errors of each model are within 7 mm/a. Compared to other models, the CS-Elman model exhibits the
smallest range of prediction absolute error, ranging from 0.071 to 1.843 mm/a. Additionally, the CS-Elman model has a
lower MAE of 0.818 mm/a and MAPE of 9.353%, both smaller than those of other models, indicating higher prediction
accuracy. Moreover, the CS-Elman model demonstrates faster convergence speed and smaller mean squared error, validating
its superiority and effectiveness in predicting surface deformation in high mountain gorge areas.

490 The CS-Elman model is superior to traditional models and is more suitable for surface deformation prediction for the
following reasons: (1) Model architecture advantage: The CS-Elman model combines the Cuckoo Search (CS) algorithm
with the Elman neural network. The CS algorithm's global search capability optimizes the Elman network's parameters,
thereby improving the model's convergence speed and prediction accuracy. (2) Nonlinear modeling capability: Unlike
traditional linear models, the CS-Elman model captures nonlinear relationships more effectively. Surface deformation is
495 often influenced by multiple complex factors, and the deep learning structure of the CS-Elman model enables it to handle
these nonlinear features effectively. (3) Adaptability and flexibility: The CS-Elman model is highly adaptable and can adjust
its parameters based on different input features, such as DEM, rainfall, and seismic activity. This allows the model to
maintain high prediction performance under various geographical and climatic conditions. (4) Comprehensive factor
evaluation: The model can consider multiple evaluation factors simultaneously, providing more comprehensive prediction
500 results. In contrast to traditional models that rely on a single or limited number of variables, CS-Elman excels in multi-factor
analysis. (5) Reliability of validation results: Experimental results show that the CS-Elman model outperforms traditional
models in terms of accuracy and stability. By comparing with InSAR monitoring results, it effectively reduces prediction
errors.

4.2.3. Deformation prediction analysis

505 Through the above experimental analysis, it has been verified that the Elman neural network optimized by the CS algorithm
has superior predictive performance. Therefore, a time-series deformation prediction is conducted on the typical deformation
points P and Q. Since the same deformation point is independent of DEM, slope, curvature, FVC, lithology and vegetation
type, time-series data such as TWI, SPI and rainfall are selected. A CS-Elman model is constructed using the time-series

deformation variables monitored by InSAR technology. A total of 26 periods (with each period being 24 days) of data from January 24, 2022 to September 16, 2023 are selected as training samples, and the CS-Elman model is used to predict the deformation values for the subsequent 4 periods. The predicted deformation values compared with the InSAR monitoring values are shown in Table 7.

Table 7: Comparison between predicted values and monitored values.

Periods		20231010	20231103	20231127	20231221
Point P	InSAR monitoring values/mm	107.391	110.315	117.408	120.557
	CS-Elman predicted values/mm	111.354	112.032	118.183	117.184
	Absolute error/mm	3.963	1.717	0.775	3.373
Point Q	InSAR monitoring values/mm	-186.347	-192.725	-194.912	-195.748
	CS-Elman predicted values/mm	-187.706	-190.148	-194.229	-200.528
	Absolute error/mm	1.359	2.577	0.683	4.780

515

According to Table 7, the average absolute errors between the predicted values and monitored values for points P and Q are 2.457 mm and 2.350 mm, respectively. According to the *Technical Specification for Ground Subsidence Measurement* (DZ/T0154-2020) released by the ministry of natural resources of China, the accuracy of InSAR deformation is ± 10 mm, and the prediction accuracy meets the requirements of the measurement specifications. Thus, it is confirmed that the combination of time-series InSAR technology and the CS-Elman algorithm can effectively monitor and predict the deformation values of points in high mountain gorges.

To validate the performance of the CS-Elman model in predicting future deformation, let the InSAR deformation time series be denoted as $h = \{h_j\}$, where $j=1, 2, \dots, n$, and b_j represents the InSAR deformation observation at time j . H and F represent the input data and predicted data, respectively. Using j consecutive subsidence observations, the subsidence at a delay of several time steps, with Delay=1, is predicted. The prediction process follows a recursive forecasting pattern, where the predicted result F from the previous time step is added to the input dataset H to form a new dataset, which is then used to predict the new F .

Based on the final deformation data from December 21, 2023, the CS-Elman model was used to obtain surface deformation predictions for the next year at points P and Q through a recursive forecasting approach, as shown in Figure 16. The CS-Elman predictions show a fluctuating trend over time. For point P, approximately six months later, the predicted values level off, indicating that deformation remains stable. For point Q, about six months later, during the rainy season, the predicted deformation trend sharply declines, which does not align with the deformation trend monitored by InSAR analysis. The results indicate that the CS-Elman model has short-term predictive capabilities but is not suitable for long-term prediction, as long-term forecasting may lead to model failure. Therefore, the proposed CS-Elman model is appropriate for short-term surface deformation prediction, with a predictive timescale of around six months. The predicted deformation can

535

be used to assist in decision-making and help prevent and mitigate geological hazards caused by surface deformation.

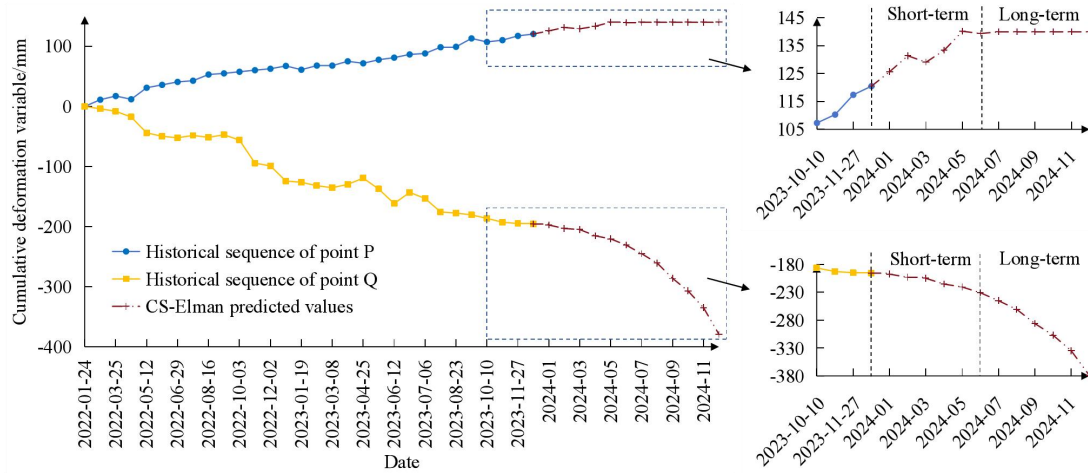


Figure 16: Predicted surface deformation results for point P and point Q for the next year (January 2024 to December 2024).

540

In this study, the CS-Elman model was used to obtain short-term surface deformation predictions for the next six months in the study area, as shown in Figure 17. Over the next six months, the maximum cumulative surface uplift in the area will reach 120.913 mm, indicating a reduction in the degree of deformation. Specifically, the upstream sections of the debris flow channels show an uplift trend, while the mid and downstream sections exhibit varying degrees of subsidence, which could lead to geological disasters with the onset of the rainy season. The short-term surface deformation predictions for the high mountain canyon area are of great significance for the prevention and control of geological disasters, such as debris flows.

545

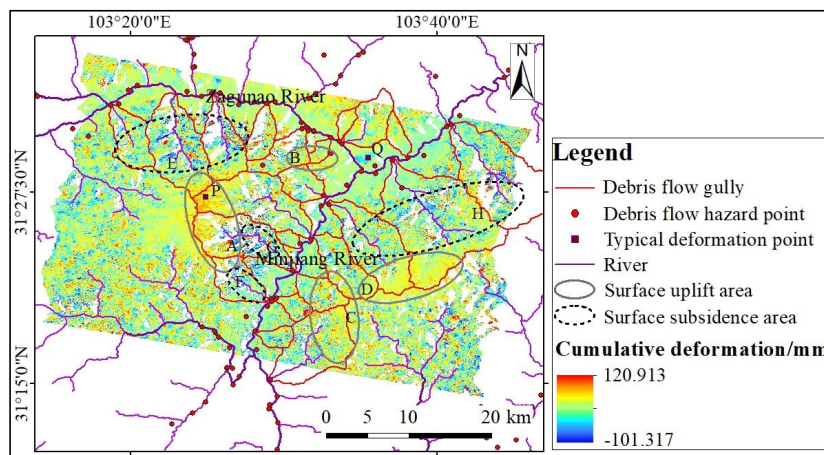


Figure 17: Predicted surface deformation results for the study area over the next six months (January 2024 to June 2024).

550

5 Conclusion

This study proposes an improved prediction method for surface deformation in high mountain gorges using the multi-factor

and multi-temporal approach based on surface deformation values monitored by time-series InSAR technology and factors such as DEM. It effectively addresses the issues of excessive dependence on deformation data and singularity in existing prediction models. Experimental comparisons reveal the following findings:

(1) The correlation coefficient R^2 between the LOS deformation velocities of the same points monitored by SBAS-InSAR and PS-InSAR technologies is 0.85, indicating a high level of correlation and demonstrating the feasibility of jointly analyzing surface deformation using these two techniques.

(2) Predictions for 30 sample sets indicate that both CS-Elman and GWO-Elman models exhibit improved performance compared to Elman alone, demonstrating that both CS and GWO algorithms effectively enhance the predictive performance and accuracy of the Elman model. Specifically, the CS-Elman model shows smaller absolute errors, fewer optimal convergence iterations, and lower mean square errors compared to the GWO-Elman network. The MAE for CS-Elman and GWO-Elman models are 1.620 mm/a and 2.155 mm/a, respectively, while the MAPE are 21.500% and 29.689%, respectively. The smaller MAE and MAPE of the CS-Elman model indicate higher prediction accuracy. This validates that utilizing the CS algorithm to improve the Elman model results in better predictive performance and effectiveness for surface deformation in high mountainous areas.

(3) By comparing the optimal CS-Elman model with SVM, LSTM and GA-BP, we verify the advantages and effectiveness of the model in predicting surface deformation in high mountainous areas. Utilizing time-series data such as TWI, SPI and rainfall, combined with the time-series deformation variables monitored by InSAR technology, the deformation trend predictions for typical deformation points P and Q show that the average absolute errors for the 4-period predictions compared to the monitored values are 2.457 mm and 2.350 mm, respectively. This validates that using time-series InSAR technology and the CS-Elman model can effectively monitor and predict the deformation values of a specific point.

(4) Based on the time series data of P point and Q point from 2022 to 2023, the CS-Elman neural network was used to predict the deformation for 2024. The analysis revealed that the CS-Elman model tends to fail in long-term predictions, particularly after six months. Therefore, the CS-Elman model is suitable for short-term predictions, with a short-term prediction scale of approximately six months. Using the CS-Elman model to forecast deformation in the study area over the next six months, the results show a maximum uplift deformation of 120.913 mm, which could trigger geological disasters due to heavy rainfall. Appropriate preventive measures should be taken.

The method in this paper validates that the CS-Elman model has a small error compared to InSAR monitoring technology and is suitable for short-term monitoring. Therefore, in practical applications, local evaluation factors such as DEM can be used as inputs to the CS-Elman model, with the annual average deformation rate as the output. Based on the IUGS/WGL (1995) geological hazard intensity classification criteria, with 2 mm/a and 16 mm/a as thresholds, regions where the predicted deformation rate exceeds 16 mm/a should be identified. Protective measures should be taken to prevent geological disasters in these areas.

585 The methodology presented in this paper, while comprehensive in considering influencing factors and time-series data, also has some limitations. For instance, the lack of concurrent leveling data prevents accurate validation of the results obtained. Moreover, the study only provides a preliminary investigation into surface deformation in the Minjiang River Basin, with limited research on typical deformation areas. Subsequent studies will further explore whether the CS-Elman model is applicable to deformation prediction in other regions. Additionally, the accuracy of time-series InSAR monitoring is significantly influenced by the resolution of the DEM. Therefore, future efforts will focus on utilizing higher-resolution DEM to enhance the accuracy of subsidence monitoring. **Additionally, we will consider factors such as distance to rivers, faults, and roads as evaluation factors in the future. We will also improve optimization algorithms like CS by incorporating long short-term memory networks (LSTM), autoregressive integrated moving average models (ARIMA), and exponential smoothing models to predict future deformation.**

595 **To address the issue of vegetation affecting the accuracy of deformation monitoring, the following measures will be taken in the future to mitigate vegetation interference: (1) Data preprocessing: Use image processing techniques, such as denoising and image segmentation, to identify and remove areas affected by vegetation interference. (2) Choosing the right timing: Collect data during different seasons of vegetation growth to select periods with minimal interference. (3) Multi-source data fusion: Combine different data sources, such as optical remote sensing and LiDAR, to improve monitoring accuracy.**

600 **Data availability**

The data that support the findings of this study are available from the corresponding author upon reasonable request.

Sentinel-1A data is acquired from the Alaska Satellite Facility (ASF) and the link is <https://search.asf.alaska.edu/#/>.

POD data is acquired from the European Space Agency (ESA) and the link is <https://step.esa.int/>.

DEM data is acquired from the Japan Aerospace Exploration Agency (JAXA) and the link is <https://www.eorc.jaxa.jp/ALOS/en/aw3d30/data/index.htm>.

605 Rainfall data is acquired from the National Earth System Science Data Center (NESSDC) and the link is <http://www.geodata.cn/data/>.

Lithology and vegetation data are acquired from the International Soil Reference and Information Centre (ISRIC) and the link is <https://www.isric.org>.

610 Soil data is acquired from the National Cryosphere Desert Data Center and the link is <https://www.ncdc.ac.cn/>.

Landsat8-9 OLT/TIRS C2 L2 data is acquired from the Geospatial Data Cloud and the link is <https://www.gscloud.cn/>.

Author contributions

Kuayue Chen: conceptualization, methodology, visualization, writing and editing. Wenfei Xi: methodology and review.

615 **Competing interests**

The contact author has declared that none of the authors has any competing interests.

Financial support

This work was supported by National Natural Science Foundation of China: [Grant Number 61966040].

References

- 620 An, B. S., Wang, W. C., Yang, W., Wu, G. J., Guo, Y. H., Zhu, H. F., Gao, Y., Bai, L., Zhang, F., Zeng, C., Wang, L., Zhou, J., Li, X., Li, J., Zhao, Z. J., Chen, Y. Y., Liu, J. S., Li, J. L., Wang, Z. Y., Chen, W. F., and Yao, T. D.: Process, mechanisms, and early warning of glacier collapse-induced river blocking disasters in the Yarlung Tsangpo Grand Canyon, southeastern Tibetan Plateau, *Sci. Total Environ.*, 816, 151652, <https://doi.org/10.1016/j.scitotenv.2021.151652>, 2022.
- Berardino, P., Fornaro, G., Lanari, R., and Sansosti, E.: A new algorithm for surface deformation monitoring based on small
625 baseline differential SAR interferograms, *IEEE T. Geosci. Remote*, 40, 2375-2383, <https://doi.org/10.1109/TGRS.2002.803792>, 2002.
- Chai, T., and Draxler, R. R.: Root mean square error (RMSE) or mean absolute error (MAE)?—Arguments against avoiding RMSE in the literature, *Geosci. Model Dev.*, 7, 1247-1250, <https://doi.org/10.5194/gmd-7-1247-2014>, 2014.
- De Myttenaere, A., Golden, B., Le Grand, B., and Rossi, F.: Mean absolute percentage error for regression models,
630 *Neurocomputing*, 192, 38-48, <https://doi.org/10.1016/j.neucom.2015.12.114>, 2016.
- Derbyshire, E.: Geological hazards in loess terrain, with particular reference to the loess regions of China, *Earth-Sci. Rev.*, 54, 231-260, [https://doi.org/10.1016/S0012-8252\(01\)00050-2](https://doi.org/10.1016/S0012-8252(01)00050-2), 2001.
- Ding, M. T., and Huang, T.: Vulnerability assessment of population in mountain settlements exposed to debris flow: a case study on Qipan gully, Wenchuan County, China, *Nat. Hazards*, 99, 553-569, <https://doi.org/10.1007/s11069-019-03759-1>,
635 2019.
- Ding, S. F., Zhang, Y. N., Chen, J. R., and Jia, W. K.: Research on using genetic algorithms to optimize Elman neural networks, *Neural Comput. Appl.*, 23, 293-297, <https://doi.org/10.1007/s00521-012-0896-3>, 2013.
- Dong, S. W., Zhang, Y. Q., Wu, Z. H., Yang, N., Ma, Y. S., Shi, W., Chen, Z. L., Long, C. X., and An, M. J.: Surface Rupture and Co-seismic Displacement Produced by the Ms 8.0 Wenchuan Earthquake of May 12th, 2008, Sichuan, China: Eastwards
640 *Growth of the Qinghai-Tibet Plateau, Acta Geol. Sin-Engl.*, 82, 938-948, <https://doi.org/10.1111/j.1755-6724.2008.tb00649.x>, 2008.

- Dziuban, C. D., and Shirkey, E. C.: When is a correlation matrix appropriate for factor analysis? Some decision rules, *Psychol. Bull.*, 81, 358, <https://doi.org/10.1037/h0036316>, 1974.
- Elman, J. L.: Finding structure in time, *Cognitive Sci.*, 14, 179-211, https://doi.org/10.1207/s15516709cog1402_1, 1990.
- 645 Ferretti, A., Prati, C., and Rocca, F.: Permanent scatterers in SAR interferometry, *IEEE T. Geosci. Remote*, 39, 8-20, <https://doi.org/10.1109/36.898661>, 2001.
- Guo, X. J., Cui, P., Li, Y., Zou, Q., and Kong, Y. D.: The formation and development of debris flows in large watersheds after the 2008 Wenchuan Earthquake, *Landslides*, 13, 25-37, <https://doi.org/10.1007/s10346-014-0541-6>, 2016.
- Gupta, S., and Deep, K.: A novel random walk grey wolf optimizer, *Swarm Evol. Comput.*, 44, 101-112, 650 <https://doi.org/10.1016/j.swevo.2018.01.001>, 2019.
- He, J., Zhang, L. M., Fan, R. L., Zhou, S. Y., Luo, H. Y., and Peng, D. L.: Evaluating effectiveness of mitigation measures for large debris flows in Wenchuan, China, *Landslides*, 19, 913-928, <https://doi.org/10.1007/s10346-021-01809-z>, 2022.
- He, M. C., Sui, Q. R., Li, M. N., Wang, Z. J., and Tao, Z. G.: Compensation excavation method control for large deformation disaster of mountain soft rock tunnel, *Int. J. Min. Sci. Techno.*, 32, 951-963, <https://doi.org/10.1016/j.ijmst.2022.08.004>, 655 2022.
- Hodson, T. O., Over, T. M., and Foks, S. S.: Mean squared error, deconstructed, *J. Adv. Model. Earth Sy.*, 13, e2021MS002681, <https://doi.org/10.1029/2021MS002681>, 2021.
- Huang Lin, C., Liu, D. W., and Liu, G.: Landslide detection in La Paz City (Bolivia) based on time series analysis of InSAR data, *Int. J. Remote Sens.*, 40, 6775-6795, <https://doi.org/10.1080/01431161.2019.1594434>, 2019.
- 660 IUGS / WGL, International Union of Geological Science Working Group on Landslides, 1995, A suggested method for describing the rate of movement of a landslide. *IAEG Bulletin*, 1995, 52, pp. 75-78.
- Jia, W. K., Zhao, D. A., Zheng, Y. J., and Hou, S. J.: A novel optimized GA–Elman neural network algorithm, *Neural Comput. Appl.*, 31, 449-459, <https://doi.org/10.1007/s00521-017-3076-7>, 2019.
- Jiang, N., Li, H. B., Li, C. J., Xiao, H. X., and Zhou, J. W.: A fusion method using terrestrial laser scanning and unmanned 665 aerial vehicle photogrammetry for landslide deformation monitoring under complex terrain conditions, *IEEE T. Geosci. Remote*, 60, 1-14, <https://doi.org/10.1109/TGRS.2022.3181258>, 2022.
- Kim, D., Langley, R. B., Bond, J., and Chrzanowski, A.: Local deformation monitoring using GPS in an open pit mine: initial study, *GPS Solut.*, 7, 176-185, <https://doi.org/10.1007/s10291-003-0075-1>, 2003.
- Li, H. R., Dai, S. L., and Zheng, J. X.: Subsidence prediction of high-fill areas based on InSAR monitoring data and the 670 PSO-SVR model, *The Chinese Journal of Geological Hazard and Control*, 35, 127-136, <https://doi.cnki.net/10.16031/j.cnki.issn.1003-8035.202210005>, 2024.
- Liao, M. S., Jiang, H. J., Wang, Y., Wang, T., and Zhang, L.: Improved topographic mapping through high-resolution SAR interferometry with atmospheric effect removal, *ISPRS J. Photogramm.*, 80, 72-79,

- <https://doi.org/10.1016/j.isprsjprs.2013.03.008>, 2013.
- 675 Liu, C. X., and Wang, B. Y.: Gully-type debris flow susceptibility assessment based on a multi-channel multi-scale residual network fusing multi-source data: a case study of Nujiang Prefecture, All Earth, 36, 1-18, <https://doi.org/10.1080/27669645.2023.2292311>, 2024.
- Liu, H., Xu, X. Y., Chen, M., Chen, F. L., Ding, R. L., and Liu, F.: Time-series InSAR-based dynamic remote sensing monitoring of the Great Wall of the Ming Dynasty in Qinhuangdao, Remote Sensing for Natural Resources, 35, 202-211, <https://doi.cnki.net/10.6046/zrzyyg.2021163>, 2023.
- 680 Mareli, M., and Twala, B.: An adaptive Cuckoo search algorithm for optimisation, Applied computing and informatics, 14, 107-115, <https://doi.org/10.1016/j.aci.2017.09.001>, 2018.
- Mirjalili, S., Mirjalili, S. M., and Lewis, A.: Grey wolf optimizer, Adv. Eng. Softw., 69, 46-61, <https://doi.org/10.1016/j.advengsoft.2013.12.007>, 2014.
- 685 Nikolaeva, E., Walter, T. R., Shirzaei, M., and Zschau, J.: Landslide observation and volume estimation in central Georgia based on L-band InSAR, Nat. Hazards Earth Syst. Sci., 14, 675-688, <https://doi.org/10.5194/nhess-14-675-2014>, 2014.
- Osmanoğlu, B., Sunar, F., Wdowinski, S., and Cabral-Cano, E.: Time series analysis of InSAR data: Methods and trends, ISPRS J. Photogramm., 115, 90-102, <https://doi.org/10.1016/j.isprsjprs.2015.10.003>, 2016.
- Parker, C., and Davey, J.: Stream power indices correspond poorly with observations of alluvial river channel adjustment, Earth Surf. Proc. Land., 48, 1290-1304, <https://doi.org/10.1002/esp.5550>, 2023.
- 690 Radman, A., Akhoondzadeh, M., and Hosseiny, B.: Integrating InSAR and deep-learning for modeling and predicting subsidence over the adjacent area of Lake Urmia, Iran, GISci. Remote Sens., 58, 1413-1433, <https://doi.org/10.1080/15481603.2021.1991689>, 2021.
- Shankar, H., Chauhan, P., Singh, D., Bhandari, R., Bhatt, C. M., Roy, A., Kannaujiya, S., and Singh, R. P. (2023). Multi-temporal InSAR and Sentinel-1 for assessing land surface movement of Joshimath town, India. Geomat. Nat. Haz. risk, 14, 2253972, <https://doi.org/10.1080/19475705.2023.2253972>, 2023.
- Suresh, D., and Yarrakula, K.: InSAR based deformation mapping of earthquake using Sentinel 1A imagery, Geocarto Int., 35, 559-568, <https://doi.org/10.1080/10106049.2018.1544289>, 2020.
- Sörensen, R., Zinko, U., and Seibert, J.: On the calculation of the topographic wetness index: evaluation of different methods based on field observations, Hydrol. Earth Syst. Sci., 10, 101-112, <https://doi.org/10.5194/hess-10-101-2006>, 2006.
- 700 Tang, C., Zhu, J., Ding, J., Cui, X. F., Chen, L., and Zhang, J. S. Catastrophic debris flows triggered by a 14 August 2010 rainfall at the epicenter of the Wenchuan earthquake, Landslides, 8, 485-497, <https://doi.org/10.1007/s10346-011-0269-5>, 2011.
- Tao, Z. G., Zhu, C., He, M. C., and Karakus, M.: A physical modeling-based study on the control mechanisms of Negative Poisson's ratio anchor cable on the stratified toppling deformation of anti-inclined slopes, Int. J. Rock Mech. Min., 138,
- 705

- 104632, <https://doi.org/10.1016/j.ijrmms.2021.104632>, 2021.
- Teng, C. Q., Wang, L., and Jiang, C.: Urban surface deformation monitoring and prediction by integrating SBAS-InSAR and Elman neural network, *Surv. Rev.*, 56, 18-31, <https://doi.org/10.1080/00396265.2022.2157119>, 2024.
- Ulusay, R., Türeli, K., and Ider, M. H.: Prediction of engineering properties of a selected litharenite sandstone from its petrographic characteristics using correlation and multivariate statistical techniques, *Eng. Geol.*, 38, 135-157, [https://doi.org/10.1016/0013-7952\(94\)90029-9](https://doi.org/10.1016/0013-7952(94)90029-9), 1994.
- Vanicek, P., Castle, R. O., and Balazs, E. I.: Geodetic leveling and its applications, *Rev. Geophys.*, 18, 505-524, <https://doi.org/10.1029/RG018i002p00505>, 1980.
- Wang, Y. Y., Guo, Y. H., Hu, S. Q., Li, Y., Wang, J. Z., Liu, X. S., and Wang, L.: Ground deformation analysis using InSAR and backpropagation prediction with influencing factors in Erhai Region, China, *Sustainability-basel*, 11, 2853, <https://doi.org/10.3390/su11102853>, 2019.
- Wang, Z. D., Wen, X. H., Tang, W., Liu, H., and Wang, D. F.: Early detection of geological hazards in Longmenshan-Dadu river area using various InSAR techniques, *Geomatics and Information Science of Wuhan University*, 45, 451-459, <https://doi.org/10.13203/j.whugis20190064>, 2020.
- Xu, F. S., and Wang, B. Y.: Debris flow susceptibility mapping in mountainous area based on multi-source data fusion and CNN model-taking Nujiang Prefecture, China as an example, *Int. J. Digit. Earth*, 15, 1966-1988, <https://doi.org/10.1080/17538947.2022.2142304>, 2022.
- Yang, X. S., and Deb, S.: Cuckoo search via Lévy flights, In 2009 World congress on nature & biologically inspired computing (NaBIC), 210-214, Ieee, <https://doi.org/10.1109/NABIC.2009.5393690>, 2009.
- Yang, Z. F., Li, Z. W., Zhu, J. J., Wang, Y. D., and Wu, L. X.: Use of SAR/InSAR in mining deformation monitoring, parameter inversion, and forward predictions: A review, *IEEE Geosc. Rem. Sen. M.*, 8, 71-90, <https://doi.org/10.1109/MGRS.2019.2954824>, 2020.
- Yang, Z. L., Lu, H., Zhang, Z. J., Liu, C., Nie, R. H., Zhang, W. C., Fan, G., Chen, C., Ma, L., Dai, X. A., Zhang, M., and Zhang, D. H.: Visualization analysis of rainfall-induced landslides hazards based on remote sensing and geographic information system-an overview, *Int. J. Digit. Earth*, 16, 2374-2402, <https://doi.org/10.1080/17538947.2023.2229797>, 2023.
- Yang, Z. R., Xi, W. F., Yang, Z. Q., Shi, Z. T., and Qian, T. H.: Monitoring and prediction of glacier deformation in the meili snow mountain based on InSAR technology and GA-BP neural network algorithm, *Sensors-basel*, 22, 8350, <https://doi.org/10.3390/s22218350>, 2022.
- Ye, Y. C., Yan, C. D., Luo, X. X., Zhang, R. F., and Yuan, G. J.: Analysis of ground subsidence along Zhengzhou metro based on time series InSAR, *National Remote Sensing Bulletin*, 26, 1342-1353, <https://doi.org/10.11834/jrs.20211246>, 2022.
- Zhang, G., Wang, S. Y., Chen, Z. W., Zheng, Y. Z., Zhao, R. S., Wang, T. Y., Zhu, Y., Yuan, X. Z., Wu, W., and Chen, W. T.: Development of China's spaceborne SAR satellite, processing strategy, and application: take Gaofen-3 series as an

example, *Geo-spat. Inf. Sci.*, 27, 221-236, <https://doi.org/10.1080/10095020.2022.2124129>, 2024.

740 Zhang, Z. J., Lin, H., Wang, M. M., Liu, X. G., Chen, Q. H., Wang, C., and Zhang, H.: A review of satellite synthetic aperture radar interferometry applications in permafrost regions: Current status, challenges, and trends, *IEEE Geosc. Rem. Sen. M.*, 10, 93-114, <https://doi.org/10.1109/MGRS.2022.3170350>, 2022.

Zhang, X. Z., Tie, Y. B., and Ning, Z. J.: Characteristics and activity analysis of the catastrophic “6·26” debris flow in the Banzi Catchment, Wenchuan County of Sichuan Province, *Hydrogeology & Engineering Geology*, 50, 134-145, <https://doi.cnki.net/10.16030/j.cnki.issn.1000-3665.202307003>, 2023.

745 Zhou, W., Tang, C., Van Asch, T. W., and Zhou, C. H.: Rainfall-triggering response patterns of post-seismic debris flows in the Wenchuan earthquake area. *Nat. Hazards*, 70: 1417-1435, <https://doi.org/10.1007/s11069-013-0883-8>, 2014.